symmetry

MDPI

Article

Small-Angle Scattering from Fractional Brownian Surfaces

Eugen Mircea Anitas [1,2]

[1] Joint Institute for Nuclear Research, 141980 Dubna, Russia; anitas@theor.jinr.ru
[2] Horia Hulubei, National Institute of Physics and Nuclear Engineering, Bucharest-Magurele, RO-077125 Bucharest, Romania

Abstract: Recent developments in nanotechnology have allowed the fabrication of a new generation of advanced materials with various fractal-like geometries. Fractional Brownian surfaces (fBs) are often used as models to simulate and characterize these complex geometries, such as the surface of particles in dilute particulate systems (e.g., colloids) or the interfaces in non-particulate two-phase systems (e.g., semicrystalline polymers with crystalline and amorphous phases). However, for such systems, a realistic simulation involves parameters averaged over a macroscopic volume. Here, a method based on small-angle scattering technique is proposed to extract the main structural parameters of surfaces/interfaces from experimental data. It involves the analysis of scattering intensities and the corresponding pair distance distribution functions. This allows the extraction of information with respect to the overall size, fractal dimension, Hurst and spectral exponents. The method is applied to several classes of fBs, and it is shown that the obtained numerical values of the structural parameters are in very good agreement with theoretical ones.

Keywords: small-angle scattering; fractional Brownian surfaces; fractal dimension; Hurst exponent; spectral exponent

Citation: Anitas, E.M. Small-Angle Scattering from Fractional Brownian Surfaces. *Symmetry* **2021**, *13*, 2042. https://doi.org/10.3390/sym13112042

Academic Editors: V. I. Yukalov, V. S. Bagnato, Rashid G. Nazmitdinov and Raffaele Barretta

Received: 15 September 2021
Accepted: 28 October 2021
Published: 30 October 2021

1. Introduction

In recent years, various advanced techniques, such as printing [1,2], gas-phase (aerosol) synthesis [3] or powder compact foaming [4], have been developed for large-scale preparation of fractal materials at nano and micro scales. An important feature for many applications is the possibility to control the surface properties of such materials and of its components as well as their symmetry and dimensionality, since it allows incorporating advanced functionalities at a design stage.

For artificially created structures, interface roughness affects coherent dynamical processes in quantum dots [5] while for solar cells, it increases their power conversion efficiency [6]. For natural rough surfaces arising in materials science, chemistry, biology or geology, the roughness is often useful for tuning superhydrophobicity [7], biocompatibility [8,9] or flexibility [7,10]. In addition to roughness, the third dimension has been proved to be important for the interpretation of experimental data on singlet-triplet transitions in the ground states of the two-electron quantum dots under a perpendicular magnetic field [11,12].

Theoretically, for both artificial and natural surfaces and interfaces, a frequently employed realistic model that aims to relate the observed physical/chemical/biological properties with the roughness is based on the concept of fractional Brownian surface (fBs) [13]. This has been successfully used in describing various rough structures, including the contact zone between two distinct materials in layered composites [14], substrates subjected to plasma-chemical etching [15] or soil structures [16,17].

A fBs is defined in terms of the Hurst exponent, and it is related to the fractal dimension [18] of the surface. This is one of the most fundamental parameters characterizing a surface since it does not depend on the sampling length or on the instrument resolution. Therefore, various methods for practical estimations of fractal dimension are commonly

used, such as the wavelet based multifractal analysis [19], the root mean square method [20], the variogram method [21], the structure function method [22] or the variation method [23].

However, for macroscopic volumes consisting of a large number of randomly distributed surfaces/interfaces, such real-space methods are not appropriate since the underlying microscopy techniques may introduce artefacts in sample preparation and can be used to provide only information for small surface areas. To overcome this issue, one can describe the average of the correlations among atoms positions by using an appropriate statistical or ensemble average of the electron density distribution within the particle [24].

In this paper, small-angle scattering (SAS) technique is used to estimate the overall shape, size and fractal dimension of 2D disordered fBs. This involves an analysis of scattering intensity $I(q)$ and its Fourier transform and the pair distance distribution function (pddf; $p(r)$). Depending on the parameters sought, either $I(q)$ or $p(r)$ may be more convenient for detailed analysis [25]. While symmetry and self-similarity characteristics provide more pronounced effects in the reciprocal space, the determination of the shape and size is more intuitive by using $p(r)$. As such, in this work, the advantages provided by both analyses are exploited.

In order to illustrate the general applicability of employing SAS technique in revealing structural properties of naturally occuring (i.e., statistically self-similar/affine) fractal surfaces/interfaces, in this work, several classes of fBs observed on a regular grid are investigated. It is shown that the obtained fractal dimensions provide values for the Hurst and spectral exponents in very good agreement with theoretical ones. The main steps on how $I(q)$ (and $p(r)$) can be employed to differentiate between various fBs are described in detail, and similarities with SAS from exact self-similar surface fractals [26–28] are highlighted.

2. Theoretical Background

SASs of X-rays (SAXS) or neutrons (SANS) are experimental techniques used for the investigation of structures with dimensions from 1 nm up to several hundreds of nanometers [29]. In the case of SAXS, the incoming wave induce dipole oscillations in the atoms, and the electrons are excited due to the high energy of X-rays. In turn, the accelerated charges generate secondary waves, which then add up at large distances and provide the scattering amplitude. This is related to the electron density distribution of the scattering object by a Fourier transform. However, in a scattering experiment, due to the high frequency, only the square of the amplitudes (scattering intensities) are recorded as a function of the scattering angle [30].

In SANS, neutrons interact with the nuclei of the atoms and with unpaired electrons, and they are sensitive to the isotopic composition of the sample. Neutrons can be used as a magnetic probe (since they posses a magnetic moment), and this allows us to investigate bulk properties of matter (due to their weak interaction with matter) [30]. In contrast to SAXS, where scattering amplitudes increase regularly with atomic number, in SANS, neutron-coherent amplitudes vary irregularly and are related by a Fourier transform to the scattering length density distribution [31].

Therefore, SAXS and SANS have their own advantages depending on the sample investigated. In particular, SANS is often used in combination with contrast-variation to probe the structure of multicomponent macromolecular complexes. In the following, the theoretical background is focused on SAXS but it applies to SANS as well when electron density is replaced by a scattering length density distribution.

2.1. Small-Angle Scattering Technique

In SAS, the differential elastic cross-section per unit angle, i.e., the scattering intensity, is obtained as the product between the scattering amplitude $A(\boldsymbol{q})$ of the irradiated volume and its complex conjugate $A(\boldsymbol{q})^*$. Here, $\boldsymbol{q}$ is the scattering vector with length $q = 4\pi\lambda^{-1}\sin\theta$, λ is the radiation wavelength and 2θ is the scattering angle. Furthermore, one considers a scattering process that involves a two-phase system consisting of a large

number of disordered particles with rough surfaces described by fBs (see below) embedded in a homogeneous matrix/solution.

Let us denote $\rho(\boldsymbol{r})$ as the electron density for a particle of volume V in a fixed orientation, i.e., the number of electrons per unit volume at position $\boldsymbol{r}$. Then, the scattered amplitude can be written as follows: $A(\boldsymbol{q}) = \int\int\int \rho(\boldsymbol{r}) \exp(-\mathrm{i}\boldsymbol{q}\cdot\boldsymbol{r})\mathrm{d}V$, where $\mathrm{d}V$ is a small volume element situated at position $\boldsymbol{r}$ and which contains $\rho(\boldsymbol{r})\mathrm{d}V$ electrons. Therefore, the scattering intensity becomes the following [30]:

$$I(\boldsymbol{q}) \equiv A(\boldsymbol{q})A(\boldsymbol{q})^* = \int\int\int \widetilde{\rho}^2(\boldsymbol{r}) \exp(-\mathrm{i}\boldsymbol{q}\cdot\boldsymbol{r})\mathrm{d}V, \tag{1}$$

where $\widetilde{\rho}^2(\boldsymbol{r}) = \int\int\int \rho(\boldsymbol{r}_1)\rho(\boldsymbol{r}_1-\boldsymbol{r})\mathrm{d}V$ is the convolution square [30,32].

In order to take into account the contribution of the matrix/solvent, the electron density in Equation (1) shall be replaced by the difference between electron densities of the particle and that of the matrix/solvent (ρ_0), i.e., by $\Delta\rho = \rho - \rho_0$. This is also known in the literature as the *contrast*. The random orientations of the particles over orientations are taken into account such that $\langle \exp(-\mathrm{i}\boldsymbol{q}\boldsymbol{r})\rangle = \sin qr/qr$. This results in the following [30]:

$$I(q) = 4\pi \int_0^\infty p(r) \frac{\sin qr}{qr} \mathrm{d}r, \tag{2}$$

where $p(r) = r^2\Delta\widetilde{\rho}^2(r)$ is the pair distance distribution function (pddf) and provides the number of different electron pairs found in the range $(r, r+\mathrm{d}r)$ within the particle. Geometrically, $p(r)$ is the distance histogram of the particle and has the property that $p(r) = 0$ at $r = 0$ and at $r > D_{\max}$, where $D_{\max}$ is the maximum dimension of the particle. For a finite number N of point-like scatterers, Equation (2) can be approximated by the following [33]:

$$I(q) = N + 2\sum_i^{N_{\mathrm{bin}}} p(r_i) \frac{\sin qr_i}{qr_i}, \tag{3}$$

where N_{bin} is the number of bins, and $p(r_i)$ is the population at pair distance r_i. This approach brings an important computational advantage since it can handle systems consisting of a large number of scatterers in reasonable timescales [33].

2.2. Small-Angle Scattering from Fractal Surfaces

Within the class of fractal surfaces, one distinguishes three main subclasses of fractals. Figure 1 provides a schematic illustration for 2D case for each subclass. The first subclass (Figure 1 left) consists of a dense object with a fractal surface. The corresponding fractal dimension of the mass is $D_{\mathrm{m}} = 2$, the fractal dimension of the surface is $1 < D_{\mathrm{s}} < 2$ and the fractal dimension of the pores (i.e., the surrounding) is $D_{\mathrm{p}} = 2$ as for the mass. When $D_{\mathrm{s}} \to 1$, the surface is perfectly smooth, while for $D_{\mathrm{s}} \to 2$, the surface is so folded that it almost completely fills the plane. They are known in the literature as surface fractals. Such surfaces are specific to erosion surfaces (materials or mountains), chemically dissolved surfaces, thin films, corrosion surfaces, fractures, etc. [34].

The second subclass (Figure 1 middle) is a fractal resembling a branched cluster or network and for which its surface is also a fractal. For this configuration, we have $D_{\mathrm{m}} = D_{\mathrm{s}} < 2$ and $D_{\mathrm{p}} = 2$. The higher the value of D_{m}, the more close the structure is, while for $D_{\mathrm{m}} \to 1$, the object becomes a line. They are known as mass fractals, and they are specific to polymer chains or various types of aggregates (carbon, soils, etc.).

The third class (Figure 1 right) is also a dense object but within which there exists a distribution of pores or holes with a fractal structure. This is called a pore fractal, and it has the properties that $D_{\mathrm{m}} = 2$ and $D_{\mathrm{s}} = D_{\mathrm{p}} < 2$. The higher the value of D_{p}, the more porous the structure becomes. As the name implies, they are specific to various porous structures, such as carbon nanopores, bituminous coals, etc.

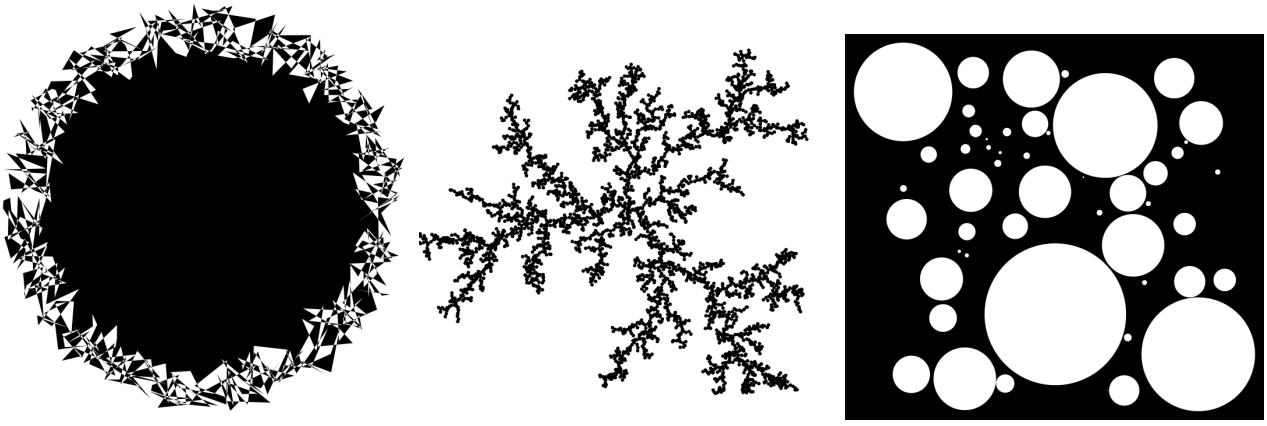

Figure 1. Schematic representation of the three main classes of fractals that can be described in a SAS experiment. (**Left**) Surface fractal ($D_m = D_p = d$ and $D_s < d$). (**Middle**) Mass fractal ($D_s = D_m < d$ and $D_p = d$). (**Right**) Pore/volume fractal ($D_s = D_p < d$ and $D_m = d$). Here, $d = 2$, and it represents the Euclidean dimension of the embedding space. See main text for details.

The fractal dimension of the fractal surface is related to the power-law behaviour of the scattering intensity (Equations (1)–(3)) by [35,36].

$$I(q) \propto q^{-\alpha}, \tag{4}$$

Here, α is the scattering exponent and carries out information about the fractal dimension: $\alpha = D_m$ for mass fractals [37], $\alpha = 4 - D_s$ [38] for surface fractals and $\alpha = D_p$ for pore fractals [39]. These relations allow inferring the type of fractal from SAS data: if the measured scattering exponent of $I(q)$ vs. q is smaller than two, then we deal with a mass fractal, while if it is higher than two (but smaller than three), we have scattering from a surface fractal [35,36].

2.3. Fractional Brownian Surfaces

Let us consider a two dimensional Euclidean space. A fBs V_H on $\mathbb{R}^2$ is a function for which its increments have a Gaussian distribution with the variance of the following [40]:

$$\left\langle |V_H(\boldsymbol{x}) - V_H(\boldsymbol{y})|^2 \right\rangle \propto |\boldsymbol{x} - \boldsymbol{y}|^{2H}, \tag{5}$$

where $\langle \cdots \rangle$ denotes an ensemble average over many samples of V_H, $0 < H < 1$ is a parameter known as a Hurst exponent and $\boldsymbol{x}, \boldsymbol{y} \in \mathbb{R}^2$. The parameter H controls the roughness of the surface: the larger its value, the smoother the surface. It is related, together with the spectral exponent β ($1 < \beta < 3$), to the fractal dimension of the surface by the following [40].

$$D = 3 - H = 2 + \frac{3 - \beta}{2}. \tag{6}$$

Here, β is useful for the determination of the spectral density or the two point autocorrelation function of V_H, which provides information about the correlations in the surface in turn.

3. Methodology for Generating the Fractional Brownian Surfaces and for Calculating the Pair Distance Distribution Function

In the present paper, fractional Brownian surfaces (fBss) are generated at different values of H (and implicitly of β) based on Equation (5) and by using the Fourier filtering method suggested in Reference [41] (Figure 2). The obtained surfaces are discretized on a rectangular grid and are recorded as elevation data relative to a plane at $z = 0$ (Figure 3). The smallest distance between grid points is denoted by l_{min}. The length of the surface in either x or y direction is denoted by a (Figure 3). In this approach, the resulting structure

is a point-like distribution similar to the one shown in the middle of Figure 1 but with "branches" not limited to a single plane. Instead, they are confined into a limited range $z_{\min} < z < z_{\max}$, where $z_{\min}$ is the lowest elevation point, and $z_{\max}$ is the highest one (see Figure 3, middle). Therefore, the model considers the space between the elevation planes (through the heights of each point relative to the $z = 0$ plane), and fBs divides this space into two non-fractal regions. This is similar to the division of the plane into two non-fractal regions by the boundary of the disk in Figure 1 (Left). This separation gives rise to surface fractals, and the parameter D in Equation (6) is related the surface fractal dimension D_s described in Section 2.2. Note that although the resulting structure is embedded in the 3D Euclidean space, the self-similarity properties are manifested only along two directions (x and y).

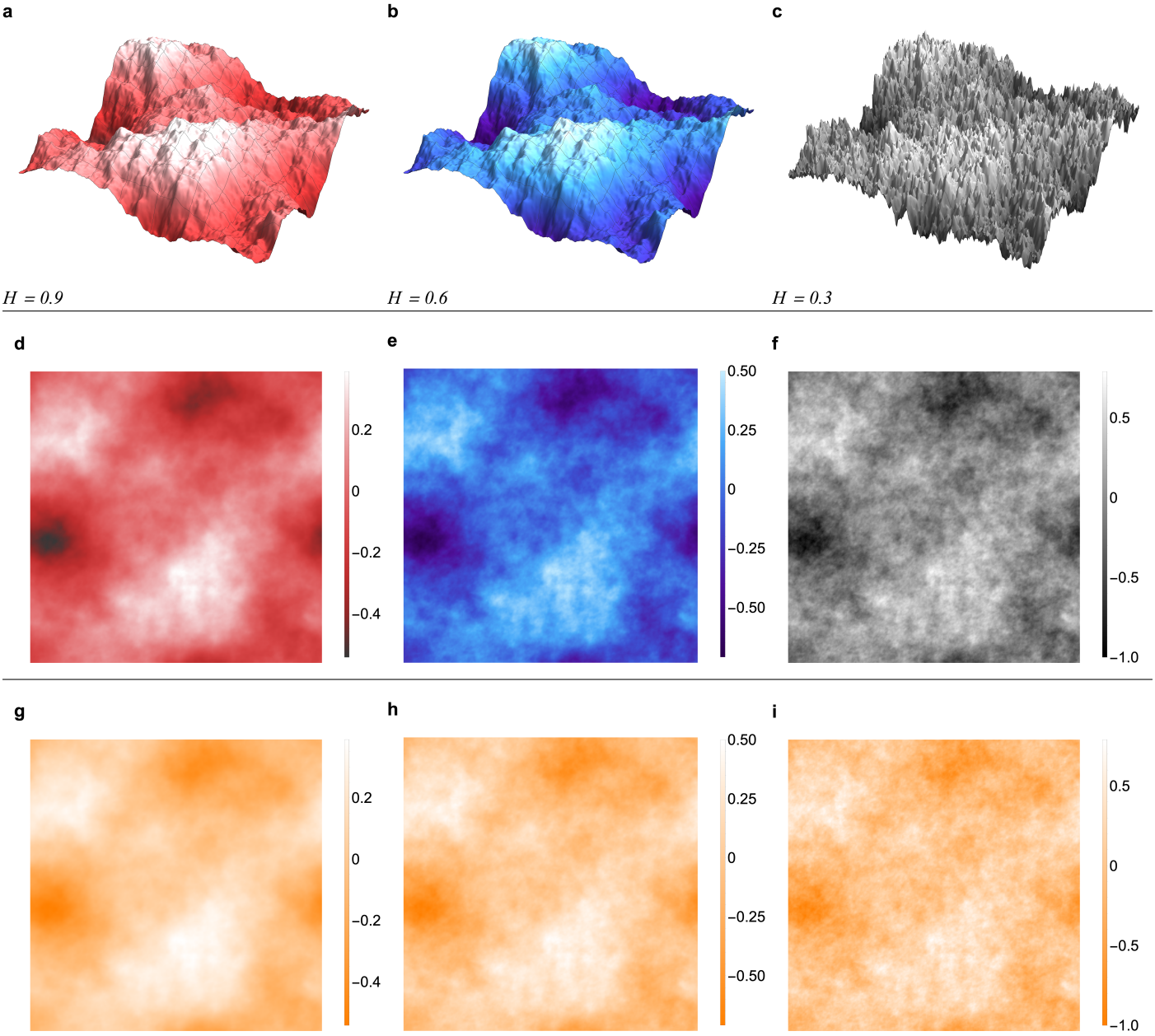

Figure 2. Fractional Brownian surfaces on a square grid with dimensions $x = y$ at various values of Hurst exponent H. (**a**–**c**) 3D representation. (**d**–**f**) Density plot. (**a**,**d**,**g**) $H = 0.9$. (**b**,**e**,**h**) $H = 0.6$. (**c**,**f**,**i**) $H = 0.3$. The peaks and bottoms are represented by light and dark regions along Oz-axis, respectively. (**g**–**i**) are the same as (**d**–**f**) but are represented in a single color for better visualization of the variation of density plot roughness. (**a**) $x \vee y = 2.31z$. (**b**) $x \vee y = 1.78z$. (**c**) $x \vee y = 1.19z$.

The geometry of the fBss, investigated here, correspond to Hurst exponents $H = 0.9$, $H = 0.6$ and, respectively, at $H = 0.3$, as shown in Figure 2. In this figure, the lighter the region, the higher the surface and vice versa. For each H, the same random seed generator was used in order to compare fBss of the same global features. As expected, the roughness of fBss increases with decreasing H (Figure 2a–c), while large scale features are preserved, i.e., the positions of maxima and minima are unchanged with H. This can be observed more clearly in the density plots in Figure 2d–f. In addition, they provide another type of method visualizing the variation of fBss roughness: the higher the value of H, the better the local variations become in terms of visibility. An equivalent representation for illustrating the differences in the local structural differences in fBss is shown in Figure 2g–i where a single color is used for all H.

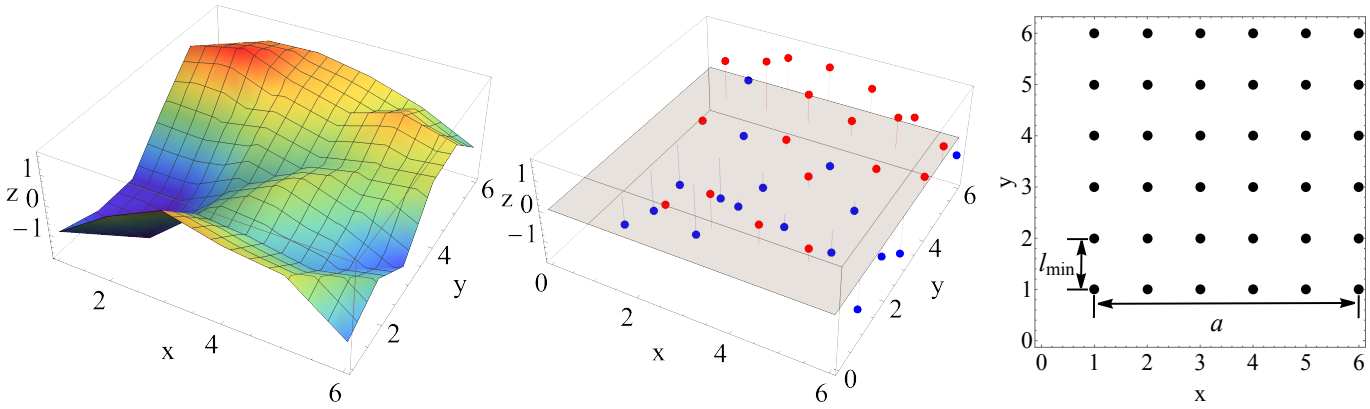

Figure 3. Schematic representation of fBS and the associated grid (6×6 points) at $H = 0.9$. (**Left**) fBs. Red—the highest points (at 1.5); Blue—the lowest ones (at -1.5). (**Middle**) The corresponding grid used. The gray plane is at $z = 0$ and stands as the reference level for the heights of the grid points. Red points are above the plane, and blue ones are below it. (**Right**) Projection of the grid on the 2D xy plane. $l_{\min}$ is the minimum distance between the points in the grid, and a is the length of the grid in either x or y direction.

Depending on their extension along x, y and z dimensions, fBss are simulated for three main cases:

- Class I fBss (CI): distances between points are kept unchanged; thus, x, y and z are of the same orders of magnitude. This corresponds to the classical structure of fBss, as shown in Figure 1, with a globular-like shape.
- Class II fBss (CII): distances between points are stretched by the same amount along x and y directions by a factor of b; thus, $x = y \ll z$. This gives rise to fBss with rectangular, planar-like shapes.
- Class III fBss (CIII): distances between points are stretched along a single direction by a factor of b; thus, x or $y \ll z$. This gives rise to fBss with rod-like shapes.

Therefore, in terms of the fractal dimension D in Equation (6) and on the classes considered above, one should expect a behaviour of scattering intensities characterized by different successions of power-law decays reflecting both the spatial and self-similarity symmetries of fBss. In particular, for the power-law decays arising from the self-similarity symmetry, one should expect a behaviour of the type $I(q) \propto q^{-D}$, where $D < 2$. Note that a random surface fractal can be built based on fBss by assigning a volume/area to each point such that their sizes follow a continuous power-law distribution similar to the case of deterministic surface fractals and where the scattering units within the fractal have a discrete power-law distribution of sizes [26,42].

The pddf $p(r)$ is calculated by using the distance histogram approach suggested in Reference [33]. This involves discretization of fBs (Figure 3, Middle), recording the position of each point and calculating all the distances between them. To this aim, the dimensions of the grid are equal to the maximum dimensions of fBs along its length, width and height.

Finally, the pair distances are discretized in a histogram of a bin size commensurate with the resolution of the data, and the scattering intensity is calculated by Equation (3) [33].

4. Results and Discussion

4.1. Pair-Distance Distribution Functions

The pair distance distribution functions (pddfs) at $H = 0.9$, $H = 0.6$ and $H = 0.3$ are calculated as described in Section 2.1 and are presented in Figure 4. The image size used for each class is 200×200 pixels, which corresponds to 4×10^4 point scatterers. For classes CII and CIII, the stretching factor is $b = 10$. Although the pddfs are different within each class, they, however, have a common feature that allows distinguishing fBss belonging to different classes. For class CI and CII (Figure 4a,b), the pddfs have a symmetric bell-like shape specific to globular or flat-like structures [30]. However, for class CIII (Figure 4c), the right side of the bell becomes completely linear, which is specific to elongated structures [30].

Within class CI, the pddfs of fBss show that the maximum diameter $D_{\max}$ occurs at $r/a \simeq 2.33$ for $H = 0.3$, $r/a \simeq 1.48$ for $H = 0.6$ and at $r/a \simeq 1.12$ at $H = 0.9$ (Figure 4a). This decrease in maximum dimension with increasing H arises from the contribution of elevation along the z-axis, since in all cases the dimensions along x and y axes are kept fixed ($a = 200 l_{\min}$). Such behaviour is in line with elevation data of fBss models as observed in the legends of Figure 2d–i. Here, the smallest difference in height occurs at $H = 0.9$, while the largest one occurs at $H = 0.3$. A second important feature of pddfs is that the position of maximum shifts to the left and increases in height with increasing H. It shows that the *value* of most common distances within fBss decreases as a consequence of decreasing elevation of points along z-axis. However, the height increases of pddf reflects an increase in the *number* of most common distances with H. Thus, the decrease in surface roughness gives rise to a larger number of point-distances with similar values. Note that the globular type of class CI fBss can be inferred also from the end region of pddf, which shows pronounced decay followed by a flat region.

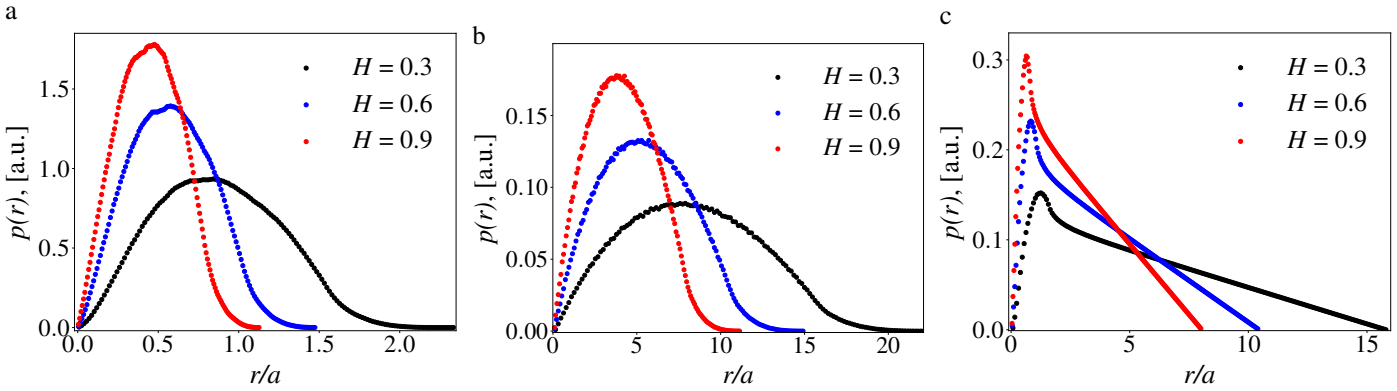

Figure 4. Pddfs from fBss at various geometries. (**a**) Class CI: symmetric bell-like curves reveal the globular-like shape. (**b**) Class CII with stretching factor $b = 10$: symmetric bell-like curves reveal planar-like structures, since one dimension is kept fixed while the other two are stretched, by a factor of $b = 10$. (**c**) Class CIII with stretching factor $b = 10$: curves with long linear domains reveal elongated structures.

The pddfs of fBss of class CII are shown in Figure 4b, and their behaviour is quite similar to fBss of class CI. However, the position and height of maxima are now related to the cross-sectional area, since they now provide the most common distances within the surface. In addition, due to the increased length sizes along x and y directions, the values of r/a at which the maximum diameter is attained also increased by a factor of b. Similarly, the number of distances decreases by a factor of b relative to fBss of class CI as a consequence of stretching the surface along the x and y directions. Note that the overall shape of the pddfs resemble quite closely those of the structures strictly confined to a plane, such as 2D DLA or surface fractals [25].

The pddfs of class CIII fBss are shown in Figure 4c and are characterized by a linear region with different slopes. One can relate it with the surface roughness of fBss: The smoother the surface, the steeper is the slope. The variation of maxima position and of its height is quite similar to class CI fBss. However, the maxima correspond to the cross section here since one can find the most common distances within them. Moreover, the curves are characterized by inflection points at $r/a \simeq 1.25$ for $H = 0.9$, $r/a \simeq 1.30$ for $H = 0.6$ and $r/a \simeq 1.35$ for $H = 0.3$, and this reveals an increase in cross-sectional area. This is also in agreement with models shown in Figure 1: The lower the H, the rougher the surface and, thus, the higher the surface area. Another particular feature for this class is that the maximum size of the surfaces significantly varies with H, i.e., $D_{\max} \simeq 16$ at $H = 0.3$, $D_{\max} \simeq 10.7$ at $H = 0.6$ and $D_{\max} \simeq 7.8$ at $H = 0.9$. One reason for this is the variation of heights along the z direction on length scales comparable with only *one* other direction (x or y). In particular, the length of z-range at $H = 0.9$ is about half of that for $H = 0.3$ (see Figure 2d,f), which is reflected in the value of their maximum sizes.

4.2. Scattering Intensities

The scattering intensities from fBss demonstrated in Figure 1 are calculated according to Equation (3) for the same classes and parameters H used for pddfs in Figure 4. The results are presented in Figure 5 on a double logarithmic scale, and they show that, within the calculated q-range, the scattering curves are characterized by the presence of a Guinier region (i.e., a region where $I(q) \propto q^0$) at $q \lesssim 2\pi/a$, followed by one or more power-law decays of the type described by Equation (4) at higher values. The scattering exponent depends on the values of H; thus, it reveals the surface roughness, while a particular succession of power-law decays or the presence of a single power-law decay is specific to the class the fBss belong to.

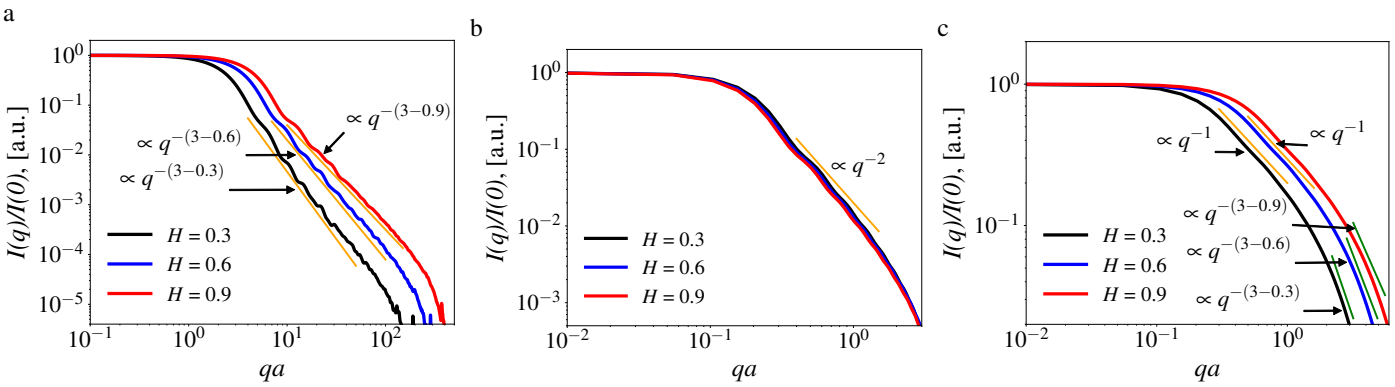

Figure 5. SAS from fBs at various grid geometries. (**a**) Three-dimensional. Fractal regions follow immediately the Guinier region (i.e., the region where $I(q) \propto q^0$) and, thus, are completely visible. (**b**) Two-dimensional. Fractal regions are expected to follow the region where $I(q) \propto q^{-2}$. (**c**) One-Dimensional. Fractal regions follow the region where $I(q) \propto q^{-1}$ and are partially visible.

The SAS intensity curves for class CI fBss are shown in Figure 5a. The results show that the length of the Guinier region increases with H and reflects the increase in the size of fBss, which is in line with the corresponding pddfs shown in Figure 4a. Then, at each H, the Guinier region is followed by a power-law decay. Here, the number of points is chosen in such a manner that the length of the power-law regimes spans at least one order of magnitude, as indicated in Reference [37]. The main feature of these power-law decays is the dependence of the scattering exponent α on H in the form $\alpha = 3 - H(\equiv D)$, and it reflects the decrease in surface roughness by decreasing the fractal dimension (see discussion in Section 2.2). This behaviour shows that the slope of scattering intensity following a power-law decay can be used to differentiate between fBss of different roughness.

For the class CII fBss, within the calculated q-range, the proposed approach show a Guinier region followed by a power-law decay $I(q) \propto q^{-2}$ for all H in the range $2\pi \lesssim qa \lesssim$

$2\pi a/d$, where $d = \sqrt{2}|z_{\max} + z_{\min}|/b$ is a measure of the size of the cross-sectional area. Here, $z_{\max}$ and $z_{\min}$ are given in the legends of Figure 1. However, since the dominant contribution comes from *equal* dimensions x and y in this configuration, the overall size changes insignificantly. Therefore, the corresponding scattering intensities in Guinier and $I(q) \propto q^{-2}$ power-law decay are very similar. Since $2\pi/d \simeq 35.9$ here is well beyond the investigated q-range, one expects that to observe more pronounced differences for $qa \gtrsim 35.9$ (see Figure 5c), which would allow revealing the fractal dimension of each fBs. This would require more extensive hardware resources than only a desktop computer.

For class CIII fBss, the Guinier region is followed first by a power-law decay $I(q) \propto q^{-1}$ in the range $2\pi \lesssim qa \lesssim 2\pi a/d$, where $d = \sqrt{2}|z_{\max} + z_{\min}|$ is a measure of the cross-section size. This is subsequently followed by a second power-law decay, which is similar to those from class I fBss. The succession of these types of power-law decays is a signature of an elongated structure with rough surfaces. Similar to the classes CI fBss, here the roughness also increases with decreasing H and is reflected in the value of the scattering exponent.

Note that for fractal surfaces with exact self-similarity, the power-law decay corresponding to the fractal region has an exponent equal to the fractal dimension of the surface. However, the simple power-law decay observed here is replaced by a succession of maxima and minima superimposed on a simple power-law decay. For such systems, the periodicity and number of these minima can be used to extract additional structural information such as the fractal iteration number or the value of the scaling factor [26–28].

5. Conclusions

The main structural properties of fBss at nano-scales and micro-scales are studied in both real and reciprocal space by exploiting the behaviour of pddfs and, respectively, of the associated small-angle scattering intensities.

The proposed approach allows us to reveal the dependence of fractal dimension and the overall size and shape of fBss on the Hurst (and implicitly, spectral) exponent. The obtained values of these structural parameters (obtained from analysis of data in Figures 4 and 5) are in a good agreement with the simulated ones (obtained from analysis of Figure 1). In particular, the simulated fractal dimensions resulting from the slope of SAS intensity at high q regions (see Figure 5) are in very good agreement with theoretical ones (given by Equation (6)).

It is shown how the SAS technique can distinguish between fBss embedded in Euclidean dimensions of different dimensionalities. The distinction is based on the presence (for flat-like and rod-like fBss) or absence (for globular-like fBss) of a succession of two power law-decays with different scattering exponents. The scattering exponent α of the first power-law is an integer reflecting the Euclidean dimensionality ($\alpha = 1$ for 1D and $\alpha = 2$ for 2D), while the scattering exponent for the second power-law is $\alpha = 3 - H$, reflecting the fractal dimension. For both power-law regions, their lower bounds allow us to determine the overall size and, respectively the cross-section size of fBs, as described in Section 4.2 *Scattering intensities*. Therefore, such a succession allows a structural characterization of fBss at various scales.

The results shown here could be a starting point for a multi-scale analysis of more complex structures involving fBss, such as mass fractals (see Figure 1 Middle) in which the branches themselves are rod-like fBss. In this case, one should expect that the first power-law decay will be replaced by a decay of the type $I(q) \propto q^{-D_m}$, where D_m is the fractal dimension of the mass fractal. Other complex geometries can be modeled by considering that the fBss form a closed surface over a domain with a given shape (i.e., ball, ellipsoid, torus, etc.).

Funding: This research received no external funding.

Institutional Review Board Statement: Not applicable.

Informed Consent Statement: Not applicable.

Data Availability Statement: Not applicable.

Conflicts of Interest: The author declares no conflict of interest.

References

1. Zeng, P.; Tian, B.; Tian, Q.; Yao, W.; Li, M.; Wang, H.; Feng, Y.; Liu, L.; Wu, W. Screen-Printed, Low-Cost, and Patterned Flexible Heater Based on Ag Fractal Dendrites for Human Wearable Application. *Adv. Mater. Technol.* **2019**, *4*, 1800453. [CrossRef]
2. Reinhardt, H.; Kroll, M.; Karstens, S.L.; Schlabach, S.; Hampp, N.A.; Tallarek, U. Nanoscaled Fractal Superstructures via Laser Patterning—A Versatile Route to Metallic Hierarchical Porous Materials. *Adv. Mater. Interfaces* **2021**, *8*, 2000253. [CrossRef]
3. Kelesidis, G.A.; Pratsinis, S.E. A perspective on gas-phase synthesis of nanomaterials: Process design, impact and outlook. *Chem. Eng. J.* **2021**, *421*, 129884. [CrossRef]
4. Liu, T.; Liu, P.; Guo, X.; Zhang, J.; Huang, Q.; Luo, Z.; Zhou, X.; Yang, Q.; Tang, Y.; Lu, A. Preparation, characterization and discussion of glass ceramic foam material: Analysis of glass phase, fractal dimension and self-foaming mechanism. *Mater. Chem. Phys.* **2020**, *243*, 122614. [CrossRef]
5. Culcer, D.; Hu, X.; Das Sarma, S. Interface roughness, valley-orbit coupling, and valley manipulation in quantum dots. *Phys. Rev. B* **2010**, *82*, 205315. [CrossRef]
6. Bonnín-Ripoll, F.; Martynov, Y.B.; Cardona, G.; Nazmitdinov, R.G.; Pujol-Nadal, R. Synergy of the ray tracing+carrier transport approach: On efficiency of perovskite solar cells with a back reflector. *Sol. Energy Mater. Sol. Cells* **2019**, *200*, 110050. [CrossRef]
7. Jiang, G.; Hu, J.; Chen, L. Preparation of a Flexible Superhydrophobic Surface and Its Wetting Mechanism Based on Fractal Theory. *Langmuir* **2020**, *36*, 8435–8443. [CrossRef]
8. Gonzalez-Torres, M.; Ramirez-Mata, A.; Melgarejo-Ramirez, Y.; Alvarez-Perez, M.A.; Jose Montesinos, J.; Leyva-Gomez, G.; Sanchez-Sanchez, R.; Eugenia-Baca, B.; Velasquillo, C. Assessment of biocompatibility and surface topography of poly(ester urethane)–silica nanocomposites reveals multifunctional properties. *Mater. Lett.* **2020**, *276*, 128269. [CrossRef]
9. Wang, Y.; Zhang, J.; Li, K.; Hu, J. Surface characterization and biocompatibility of isotropic microstructure prepared by UV laser. *J. Mater. Sci. Technol.* **2021**, *94*, 136–146. [CrossRef]
10. Vipul, S.; Anastasia, K.; Kyriacos, Y.; Kimmo, L.; Veikko, S. Flexible biodegradable transparent heaters based on fractal-like leaf skeletons. *NPJ Flex. Electron.* **2020**, *4*, 27. [CrossRef]
11. Nazmitdinov, R.G.; Simonović, N.S.; Rost, J.M. Semiclassical analysis of a two-electron quantum dot in a magnetic field: Dimensional phenomena. *Phys. Rev. B* **2002**, *65*, 155307. [CrossRef]
12. Nazmitdinov, R.G.; Simonović, N.S. Finite-thickness effects in ground-state transitions of two-electron quantum dots. *Phys. Rev. B* **2007**, *76*, 193306. [CrossRef]
13. Mandelbrot, B.B.; Van Ness, J.W. Fractional Brownian Motions, Fractional Noises and Applications. *SIAM Rev.* **1968**, *10*, 422–437. [CrossRef]
14. Calame, J.P.; Garven, M. Dielectric permittivity simulations of layered composites with rough interfacial surfaces. *IEEE Trans. Dielectr. Electr. Insul.* **2007**, *14*, 287–295. [CrossRef]
15. Glyanko, M.S.; Volkov, A.V.; Fomchenkov, S.A. Assessment of surface roughness of substrates subjected to plasma-chemical etching. *J. Phys. Conf. Ser.* **2014**, *541*, 012100. [CrossRef]
16. Zribi, M.; Ciarletti, V.; Taconet, O.; Paillé, J.; Boissard, P. Characterisation of the Soil Structure and Microwave Backscattering Based on Numerical Three-Dimensional Surface Representation: Analysis with a Fractional Brownian Model. *Remote Sens. Environ.* **2000**, *72*, 159–169. [CrossRef]
17. Clivati-McIntyre, A.A.; McCoy, E.L. Fractional Brownian description of aggregate surfaces within undisturbed soil samples using penetration resistance measurements. *Soil Tillage Res.* **2006**, *88*, 144–152. [CrossRef]
18. Mandelbrot, B.B. *The Fractal Geometry of Nature*; W.H. Freeman: San Francisco, CA, USA, 1982; p. 460.
19. Arrault, J.; Arnéodo, A.; Davis, A.; Marshak, A. Wavelet Based Multifractal Analysis of Rough Surfaces: Application to Cloud Models and Satellite Data. *Phys. Rev. Lett.* **1997**, *79*, 75–78. [CrossRef]
20. Majumdar, A.; Tien, C. Fractal characterization and simulation of rough surfaces. *Wear* **1990**, *136*, 313–327. [CrossRef]
21. Liang, X.; Lin, B.; Han, X.; Chen, S. Fractal analysis of engineering ceramics ground surface. *Appl. Surf. Sci.* **2012**, *258*, 6406–6415. [CrossRef]
22. Liu, Y.; Wang, Y.; Chen, X.; Zhang, C.; Tan, Y. Two-stage method for fractal dimension calculation of the mechanical equipment rough surface profile based on fractal theory. *Chaos Solitons Fractals* **2017**, *104*, 495–502. [CrossRef]
23. Dubuc, B.; Zucker, S.W.; Tricot, C.; Quiniou, J.F.; Wehbi, D.; Berry, M.V. Evaluating the fractal dimension of surfaces. *Proc. R. Soc. Lond. A Math. Phys. Sci.* **1989**, *425*, 113–127. [CrossRef]
24. Schaefer, D.W.; Justice, R.S. How Nano Are Nanocomposites? *Macromolecules* **2007**, *40*, 8501–8517. [CrossRef]
25. Anitas, E.M. Small-Angle Scattering from Fractals: Differentiating between Various Types of Structures. *Symmetry* **2020**, *12*, 65. [CrossRef]
26. Cherny, A.Y.; Anitas, E.M.; Osipov, V.A.; Kuklin, A.I. Small-angle scattering from the Cantor surface fractal on the plane and the Koch snowflake. *Phys. Chem. Chem. Phys.* **2017**, *19*, 2261–2268. [CrossRef]
27. Anitas, E.M.; Slyamov, A.; Szakacs, S. Microstructural characterization of surface fractals using small-angle scattering. *Rom. J. Phys.* **2018**, *63*, 104.

28. Cherny, A.Y.; Anitas, E.M.; Osipov, V.A.; Kuklin, A.I. The structure of deterministic mass and surface fractals: Theory and methods of analyzing small-angle scattering data. *Phys. Chem. Chem. Phys.* **2019**, *21*, 12748–12762. [CrossRef] [PubMed]
29. Feigin, L.A.; Svergun, D.I. *Structure Analysis by Small-Angle X-ray and Neutron Scattering*; Springer: Boston, MA, USA, 1987; p. 335. [CrossRef]
30. Glatter, O.; May, R. Small-Angle Techniques. In *International Tables for Crystallography Volume C: Mathematical, Physical and Chemical Tables*; Prince, E., Ed.; Springer: Dordrecht, The Netherland, 2004; pp. 89–112.
31. Bacon, G.E. *Neutron Diffraction*, 2nd ed.; Oxford University Press: London, UK, 1962; p. 438.
32. Bracewell, R. *The Fourier Transform and Its Applications*, 3rd ed.; Mcgraw-Hill College: Singapore, 2000; p. 486.
33. Pantos, E.; Bordas, J. Supercomputer simulation of small angle X-ray scattering, electron micrographs and X-ray diffraction patterns of macromolecular structures. *Pure Appl. Chem.* **1994**, *66*, 77–82. [CrossRef]
34. Russ, J.C. *Fractal Surfaces*; Springer Science + Business Media: Raleigh, NC, USA, 1994; p. 309. [CrossRef]
35. Martin, J.E.; Hurd, A.J. Scattering from fractals. *J. Appl. Crystallogr.* **1987**, *20*, 61–78. [CrossRef]
36. Schmidt, P.W. Small-angle scattering studies of disordered, porous and fractal systems. *J. Appl. Crystallogr.* **1991**, *24*, 414–435. [CrossRef]
37. Teixeira, J. Small-angle scattering by fractal systems. *J. Appl. Crystallogr.* **1988**, *21*, 781–785. [CrossRef]
38. Bale, H.D.; Schmidt, P.W. Small-Angle X-Ray-Scattering Investigation of Submicroscopic Porosity with Fractal Properties. *Phys. Rev. Lett.* **1984**, *53*, 596–599. [CrossRef]
39. Pfeifer, P.; Ehrburger-Dolle, F.; Rieker, T.P.; González, M.T.; Hoffman, W.P.; Molina-Sabio, M.; Rodríguez-Reinoso, F.; Schmidt, P.W.; Voss, D.J. Nearly Space-Filling Fractal Networks of Carbon Nanopores. *Phys. Rev. Lett.* **2002**, *88*, 115502. [CrossRef] [PubMed]
40. Stein, M.L. Fast and Exact Simulation of Fractional Brownian Surfaces. *J. Comput. Graph. Stat.* **2002**, *11*, 587–599. [CrossRef]
41. Saupe, D. Algorithms for random fractals. In *The Science of Fractal Images*; Peitgen, H.O., Saupe, D., Eds.; Springer: New York, NY, USA, 1988; pp. 71–113.
42. Cherny, A.Y.; Anitas, E.M.; Osipov, V.A.; Kuklin, A.I. Scattering from surface fractals in terms of composing mass fractals. *J. Appl. Crystallogr.* **2017**, *50*, 919–931. [CrossRef]